THE JOURNAL OF PHYSICAL CHEMISTRY B

Article

pubs.acs.org/JPCB

Absolute Configuration Determination of a Taxol Precursor Based on Raman Optical Activity Spectra

Václav Profant,*[,†] Alexandr Jegorov,[‡] Petr Bouř,*[,§] and Vladimír Baumruk[†]

[†]Institute of Physics, Faculty of Mathematics and Physics, Charles University, Ke Karlovu 5, 121 16 Prague 2, Czech Republic

[‡]Teva Czech Industries s.r.o., Branišovská 31, 370 05 České Budějovice, Czech Republic

[§]Institute of Organic Chemistry and Biochemistry, Academy of Sciences, Flemingovo n. 2, 166 10 Prague 6, Czech Republic

ABSTRACT: Enantiomeric purity of drugs is essential for their biological activity. In the present study, we investigate the performance of Raman optical activity (ROA) spectroscopy in distinguishing four possible stereoisomers of the synthetic precursor used for the production of taxol from baccatin III. Taxol is one of the best-selling medicaments used in the treatment of ovarian, lung, and breast cancers and Kaposi's sarcoma. In a low yield, it may be isolated from the bark of the Pacific yew tree (*Taxus brevifolia*); however, its industrial production is largely dependent on the precursor. It is shown that for reliable comparison of the experimental and computed Raman and ROA intensities a large number of conformers had to be averaged, to properly account for molecular flexibility in solution. In addition, if combined with the density functional theory computations, ROA spectra provide convenient and economic means of absolute configuration determination.

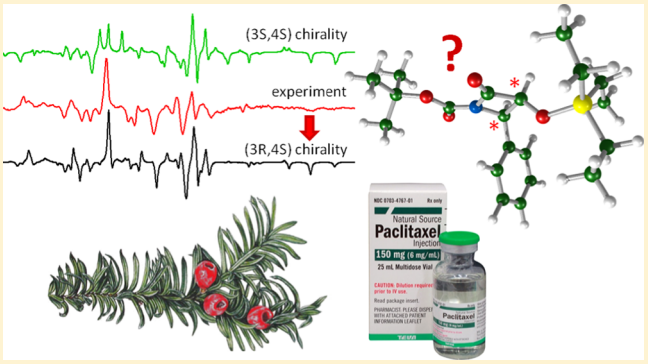

INTRODUCTION

Paclitaxel, also known as Taxol, is one of the most powerful natural anticancer agents. It is one of the best-selling medicaments used in the treatment of ovarian, lung, and breast cancers as well as Kaposi's sarcoma.[1] It was discovered in the bark of western yew, *Taxus brevifolia*, at the Research Triangle Institute in North Carolina in 1967; its chemical structure was first published in 1971[2] (see Figure 1, left). It was promptly found that paclitaxel acts as a mitotic inhibitor of cell division; its unique mechanism of action was discovered in 1979.[3] Paclitaxel also targets tubuline, causing defects in mitotic spindle assembly and chromosome segregation. Unlike other antimitotic agents, which prevent the polymerization of tubulin into microtubules (colchicine, vinca alcaloids, etc.),[4] paclitaxel stabilizes the microtubule polymer, which prevents the metaphase spindle configuration in chromosomes and eventually leads to cell apoptosis.[5,6]

Chemically, paclitaxel is classified as a taxane diterpenoid or taxoid.[4] Such diterpenoids comprise over 200 compounds and possess a skeleton of 20 carbon atoms, forming four isoprene units. They share the [9.3.1.0] pentadecene system,[7] forming three rings (A, B, and C; Figure 1). Paclitaxel is an ester having an *N*-benzoylphenyl-isoserine group attached at C13 and an extra oxetane D ring attached at C4 and C5. There are 11 stereocenters in the molecule; the natural one is displayed in Figure 1.[2]

Paclitaxel may be isolated from the bark of the Pacific yew tree (*T. brevifolia*), but the tree is rather rare and the content of the compound is low (0.1 g/kg).[2] Once the bark is removed, the tree dies. The demand for paclitaxel brought about a tremendous effort to obtain this molecule synthetically. Total synthesis of paclitaxel was first reported in 1994.[8−11] However, commercial production in this manner is not economical and semi-synthetic approaches based on chemical modifications of natural taxoids have been pursued instead.

Some of them[12] are based on the chemical functionalization of baccatin III (Figure 2), which could be isolated from the leaves of a common European yew tree, *Taxus baccata* (1 g/kg). Removal of the leaves from the tree has no effect on its health, and the leaves are quickly replaced by the plant. Baccatin III differs from paclitaxel in the presence of an OH group at C13 instead of the Taxol side chain.

Therefore, baccatin III is functionalized by 1-*t*-butyloxycarbonyl-3-triethylsilyloxy-4-phenyl-2-azetidinone (1-BOC-3-TES-4-Ph-azetidin-2-one, **I** in Figure 3), possessing two chiral centers. Among the four possible stereoisomers of **I**, just one of them, (3*R*,4*S*)-**I**, can be used. Therefore, there is a need for unambiguous and relatively easy differentiation among them. Standard ways of assigning the absolute configuration comprise X-ray crystallography and NMR. However, they are quite laborious, for example, requiring either crystallization or chemical derivatization. We investigate the reliability of Raman optical activity (ROA)[13−15] spectroscopy in assigning the absolute configuration. ROA spectroscopy together with vibrational circular dichroism (VCD) spectroscopy[16−18] explores the

Received: December 7, 2016
Revised: January 20, 2017
Published: January 22, 2017

DOI: 10.1021/acs.jpcb.6b12318
J. Phys. Chem. B 2017, 121, 1544−1551

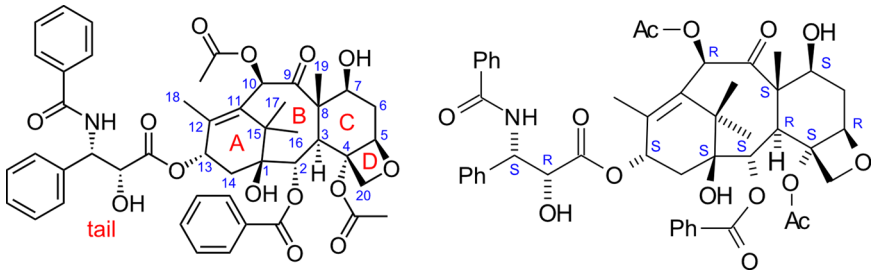

Figure 1. Structure of paclitaxel, with labeled rings and the numbering scheme of the [9.3.1.0] pentadecene system (left). Chiral centers of a pharmaceutically active stereoisomer of paclitaxel (right).

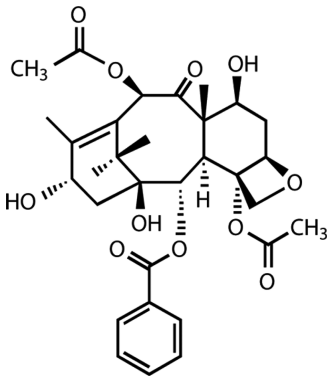

Figure 2. Structure of baccatin III.

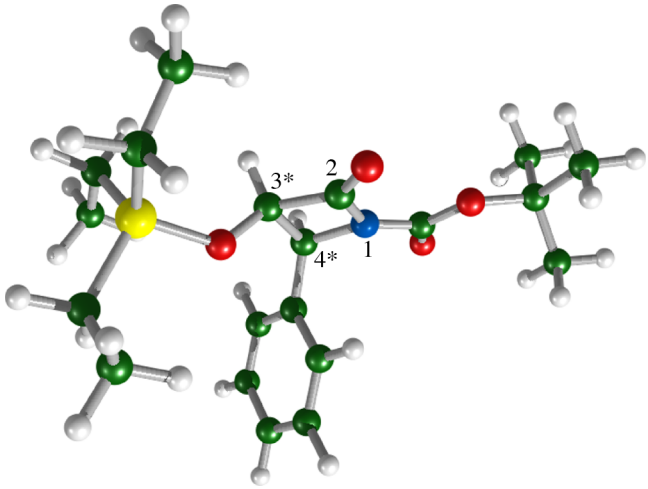

Figure 3. Structure of (3*R*,4*S*)-**I**, with labeled numbering of the azetidine ring. Chiral carbon atoms are marked by asterisks.

natural vibrational optical activity[19] of molecules. These techniques are very sensitive to stereochemistry and conformation and were thus advertised as ideal techniques for determining the absolute configuration[20] and enantiomeric purity. They can also identify the conformation of biological molecules in solution (peptides,[21−25] proteins,[26−28] nucleic acids,[29,30] carbohydrates,[31−33] viruses,[34] etc.).

Because of the limited spectral range of the VCD technique, we focus on spectroscopic differentiation among individual stereoisomers of **I** using the ROA method, combining the experimental data with density functional theory (DFT) simulations.

METHODS

Experimental Section. Two samples (marked as A and B) with different, but unknown, absolute configurations of **I** were provided by Teva Pharmaceuticals CZ, s.r.o. and dissolved in MetOH to a concentration 50 mg/ml. Each solution was put into

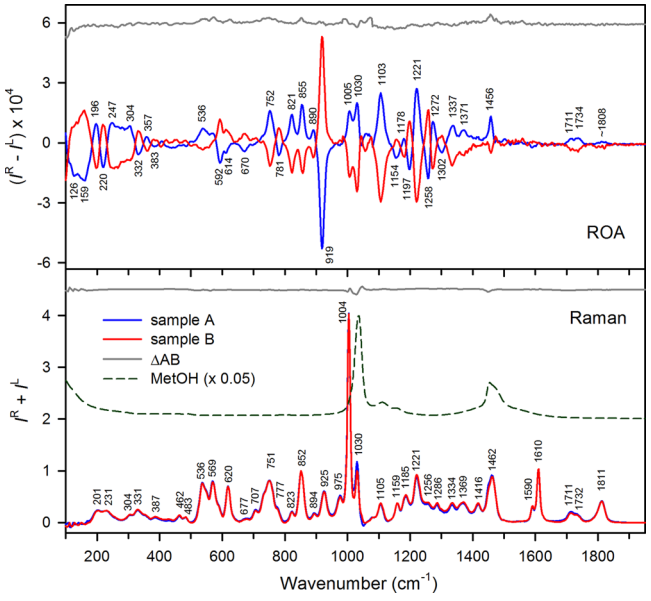

Figure 4. Experimental Raman and ROA experimental spectra of samples A and B of **I**. Differences, $\Delta AB_{RAM} = (A_{RAM} - B_{RAM})/2$ and $\Delta AB_{ROA} = (A_{ROA} + B_{ROA})/2$, and solvent (MetOH) spectra are also plotted.

a quartz cell (~60 μl, 4 × 3 mm; Starna Scientific Ltd.) and measured at room temperature (20 °C). Before signal accumulation, the samples were left in the laser beam for 30 min to quench the fluorescence from residual impurities. Raman and ROA spectra were recorded using a μ-ChiralRaman-2X instrument (BioTools, Inc.) within a spectral range of 100−2455 cm^{-1}, with a 532 nm excitation wavelength, 1.029 s accumulation time, and 8 cm^{-1} resolution and for 10 min per frame (480 accumulations). The total acquisition time of each sample was ~80 h. The wavenumber scale was calibrated using the Raman spectrum of toluene. The Raman spectrum of the MetOH solvent was accumulated for 20 min and subtracted as a baseline; the final spectra were also smoothed to eliminate instrumental noise. The ROA spectra required only minor polynomial baseline adjustment. Spectral intensities were corrected for the instrument response function.[35]

Quantum Mechanical Calculations. Structure optimization was done using the Gaussian09 (Revision B01) program,[36]

DOI: 10.1021/acs.jpcb.6b12318
J. Phys. Chem. B 2017, 121, 1544−1551

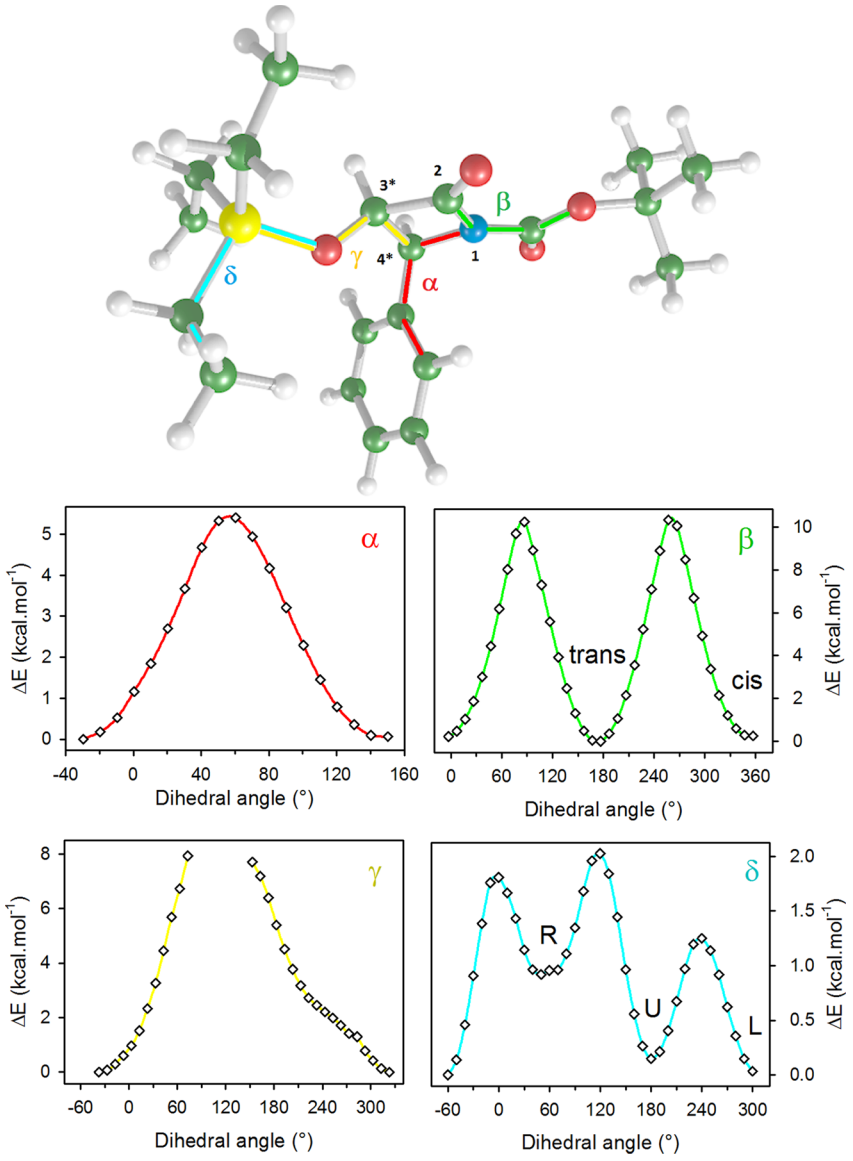

Figure 5. Definition of the dihedral angles in the (3*R*,4*S*)-**I** conformer (top) and corresponding calculated potential energy profiles (bottom). Multiple minima are labeled.

using the B3LYP hybrid functional,[37,38] 6-311++G** basis set,[39] and implicit solvent model COSMO[40,41] to mimic the MetOH environment. The starting conformations were generated by scanning (10° step) four dihedral angles (see Figure 5 for their definitions) using a smaller basis set (6-31G).

Raman and ROA intensities for individual conformers were obtained within the harmonic approximation at the same level of theory (DFT/B3LYP/6-311++G**/COSMO(MetOH)); back-scattered spectral profiles were generated by convolution of the intensities with a Lorentzian function of 10 cm^{-1} full width at half-height and a Boltzmann factor corresponding to 298 K. Spectra of each diastereomer were acquired as a Boltzmann average corresponding to DFT energies. We used various weightings based on the electronic energy (ΔE), zero-point vibrational energy (ΔE_0), enthalpy (ΔH), and Gibbs energy (ΔG).

RESULTS AND DISCUSSION

Experimental Raman and ROA Spectra. The experimental spectra are shown in Figure 4. The Raman spectra of both enantiomers look almost identical, indicating a high purity of the samples. The largest difference in the Raman spectra, ΔAB_{RAM}, can be seen around 1030 and 1460 cm^{-1}, where intense MetOH solvent bands occur and the baseline is difficult to subtract. Note that the intensity ratio of the solvent-to-solute signal was ~15–30:1. The "identical" Raman spectra also indicate that samples A and B have the same or opposite (enantiomeric) configurations, that is, they are not diastereomers. This is obviously confirmed by the ROA spectra, exhibiting a "mirror-image" symmetry. From the ROA spectra, we can also tell that the enantiomeric excess is comparable, most probably close to 100%.

Conformer Analysis. The azetidine ring in **I** is quite rigid; however, the orientation of the lateral groups (BOC, TES, and Ph), dependent on dihedral angles α, β, γ, and δ, can vary. One-dimensional scans that allow us to better estimate the molecular flexibility are plotted in Figure 5.

For the Ph group, there is only one favored orientation, at $\alpha \sim -30°$. The BOC group prefers two different orientations, with β's of −5° and 175° (cis and trans). There is also considerable freedom in the conformations of the TES ethyl groups, with

DOI: 10.1021/acs.jpcb.6b12318
J. Phys. Chem. B 2017, 121, 1544−1551

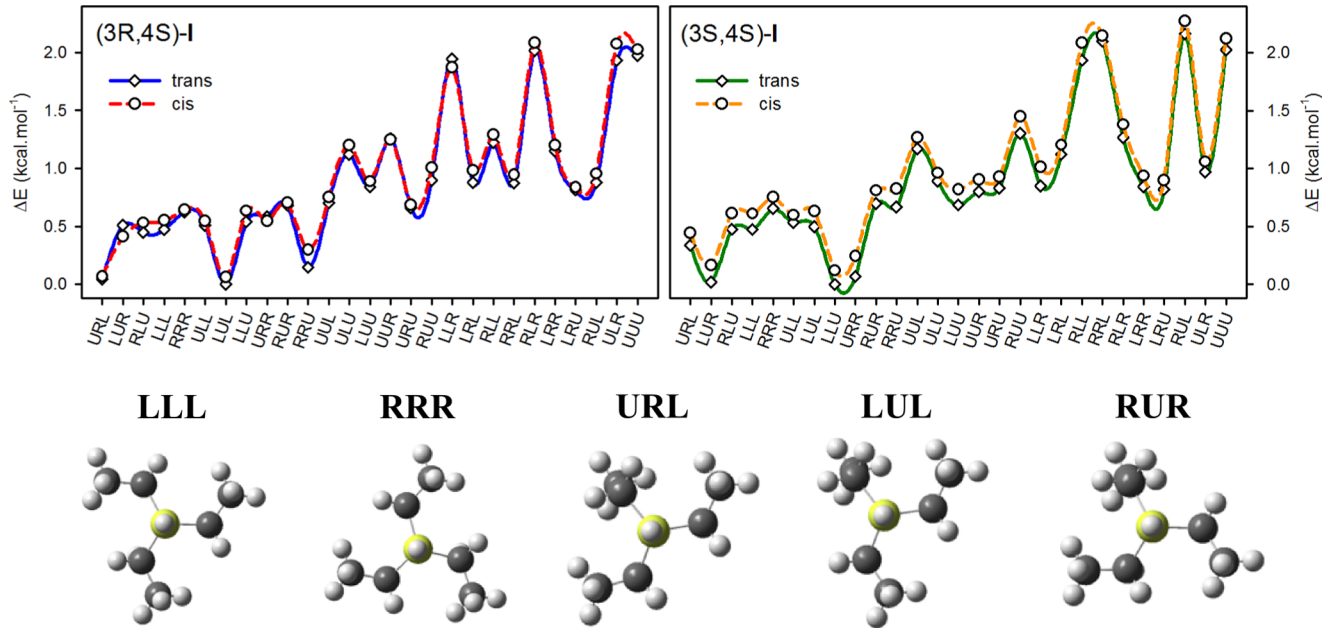

Figure 6. Relative energies of (3*R*,4*S*)-**I** conformers, and the most favored conformations of the TES group.

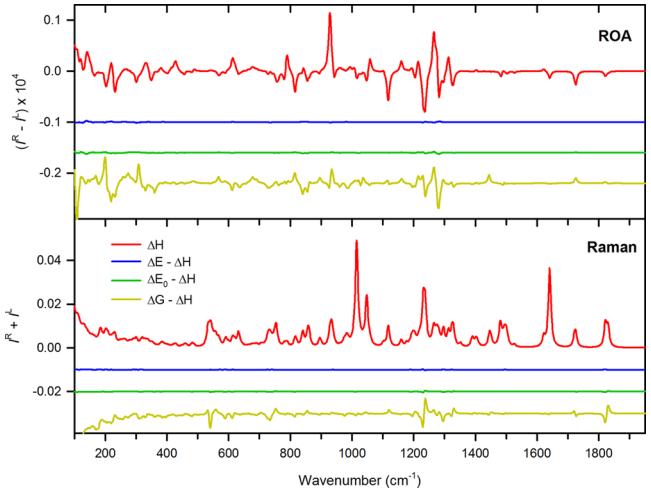

Figure 7. Raman and ROA spectra of (3*R*,4*S*)-**I**. Spectra based on Δ*H* Boltzmann weighting are plotted in red. Averaging schemes based on the Δ*E*, ΔE_0, and Δ*G* energies provided very similar spectral profiles; therefore, we plot only their differences with respect to the Δ*H* curve, marked as "Δ*E* − Δ*H*" (blue), "ΔE_0 − Δ*H*" (green), and "Δ*G* − Δ*H*" (yellow).

three stable orientations, L ($\delta \sim -60°$), R ($\delta \sim 60°$), and U ($\delta \sim 180°$), which lead to 27 different conformations for the whole TES group. Thus, in total, 54 conformers were considered. Their calculated relative energies are shown in Figure 6 for (3*R*,4*S*)-**I**. We can see that the orientations of the BOC and TES groups contribute almost independently, as the curves specific to each conformation of the BOC group (cis or trans) are similar. The trans conformation is slightly preferred over the cis conformation (by about ~0.07 kcal.mol^{-1}) due to steric reasons, that is, the proximity of the Ph group. Rotation of the ethyl groups causes energy changes up to 2.2 kcal/mol. The lowest-energy conformations with respect to the TES group ethyls are LLL, RRR, URL, LUL, and RUR (Figure 6).

As the relative energy differences are close to the Boltzmann quantum ($kT \sim 0.6$ kcal/mol at 20 °C) all 54 conformers can, in principle, contribute to the spectra, and we average the results for all of them.

Table 1. Calculated Boltzmann Weights (Based on Δ*H*) of the (3*R*, 4*S*)-I Conformers at 300 K

conformation		(3*R*,4*S*)-**I**	conformation		(3*R*,4*S*)-**I**
BOC	TES	*n* (%)	BOC	TES	*n* (%)
A	URL	**5.5**[a]	B	URL	**5.3**
	LUR	**2.6**		LUR	**3.0**
	RLU	**2.8**		RLU	2.5
	LLL	**2.7**		LLL	2.4
	RRR	2.1		RRR	2.1
	ULL	2.5		ULL	2.4
	LUL	**6.0**		LUL	**5.4**
	LLU	2.4		LLU	2.1
	URR	2.3		URR	2.4
	RUR	1.9		RUR	1.9
	RRU	**4.7**		RRU	**3.6**
	UUL	1.9		UUL	1.7
	ULU	0.9		ULU	0.8
	LUU	1.5		LUU	1.4
	UUR	0.7		UUR	0.7
	URU	2.0		URU	1.9
	RUU	1.3		RUU	1.1
	LLR	0.2		LLR	0.3
	LRL	1.4		LRL	1.2
	RLL	0.8		RLL	0.7
	RRL	1.4		RRL	1.2
	RLR	0.2		RLR	0.2
	LRR	0.9		LRR	0.8
	LRU	1.5		LRU	1.5
	RUL	1.4		RUL	1.2
	ULR	0.2		ULR	0.2
	UUU	0.2		UUU	0.2

[a]The bold values correspond to the 10 most abundant conformers.

Calculated Raman and ROA Spectra. The spectral profiles were calculated as a Boltzmann average. The Δ*E*, ΔE_0, and Δ*H*

DOI: 10.1021/acs.jpcb.6b12318
J. Phys. Chem. B 2017, 121, 1544−1551

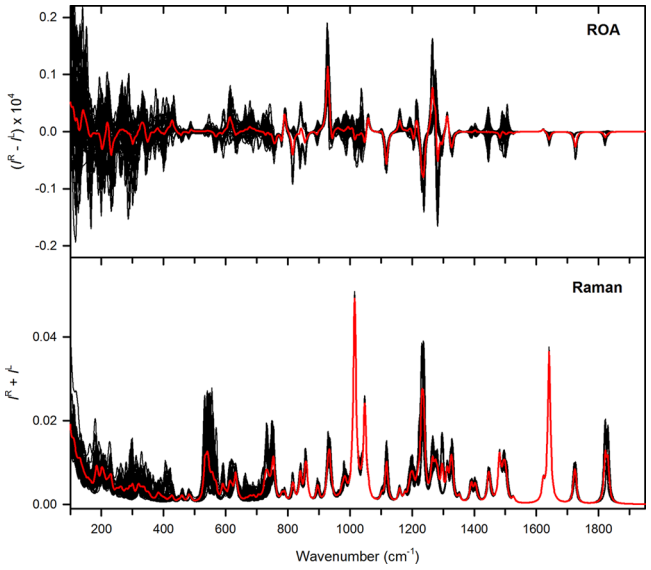

Figure 8. Calculated Raman and ROA spectra of (3*R*,4*S*)-**I** conformers and the Boltzmann average (Δ*H*; for individual conformer weights, see Table 1).

energy models provided almost identical results, whereas Δ*G* gave slightly different spectra (Figure 7). Further, we use Δ*H* weighting (see Table 1), as the Δ*G* model implemented in Gaussian for the gas phase might not be applicable to our system

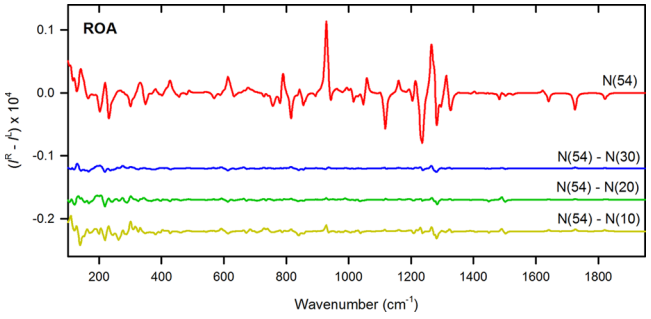

Figure 9. ROA spectrum of (3*R*,4*S*)-**I**, calculated as the Δ*H*-based Boltzmann average obtained from the full set of 54 conformers ("*N*(54)", red), and differential spectra with respect to the spectra obtained by averaging only 30, 20, and 10 conformers ("*N*(54) − *N*(30)", blue; "*N*(54) − *N*(20)", green; and "*N*(54) − *N*(10)", yellow, respectively).

and because of the numerical instability of Δ*G* for low-frequency vibrations.

Individual conformer intensities are shown in Figure 8. In the Raman spectra, the averaging results merely in broadening of the spectral lines. For the ROA spectra, the differences between the conformers are much larger and averaging is needed for modeling of the observed intensities. Note, for example, the cancelation of the signals between 1400 and 1500 cm^{-1}, formation of the (+−+-)-pattern around 800 cm^{-1}, and buildup of the average signal bellow 400 cm^{-1}. Thus, the ROA spectra seem to be more sensitive to the conformer composition of the sample at least on a qualitative level.

The effect of the number of conformers used in Boltzmann averaging on the ROA spectrum is shown in Figure 9. Obviously, high-energy conformers ($N > 20$) do not contribute much; the difference becomes more significant only when $N = 10$

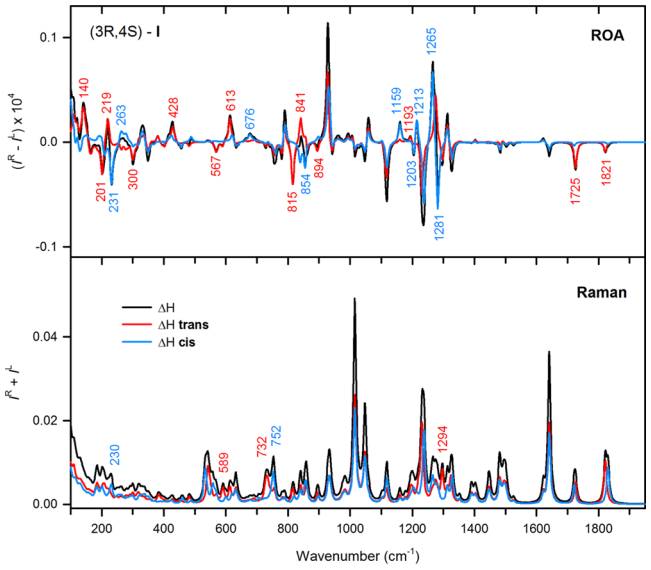

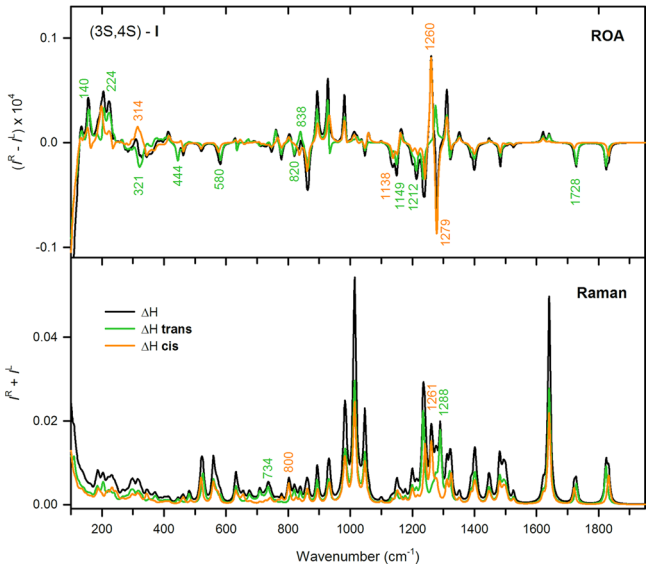

Figure 10. Raman and ROA spectra of the A and B conformers of (3*R*,4*S*)-**I** (top) and (3*S*,4*S*)-**I** (bottom), otherwise calculated as a Boltzmann average (Δ*H*) over TES ethyl group orientations. Summary Raman and ROA spectra are shown in black; marker bands for the cis or trans conformation of the BOC group are labeled.

conformers are used. Even then, the spectrum is very similar to the full average.

Although only the average is observable, to obtain a detailed view of ROA structural sensitivity it is interesting to analyze the contributions of several prominent conformations. For example, the cis and trans conformations of the BOC group affect different **I** diastereomers differently, as shown in Figure 10. The differences are much more obvious in the ROA spectra than in the Raman spectra, which is shown on the number of labeled bands specific to each conformation.

Absolute Configuration Determination. Raman and ROA spectra of the (3*R*,4*S*)-**I** and (3*S*,4*S*)-**I** diastereoisomers are compared in Figure 11. The calculated spectra seem to exhibit a sufficient number of differences for reliable assignment of the absolute configuration when compared with the experimental spectra. The most important criterion is correspondence of the signs of the ROA spectral bands. The calculated band positions

DOI: 10.1021/acs.jpcb.6b12318
J. Phys. Chem. B 2017, 121, 1544−1551

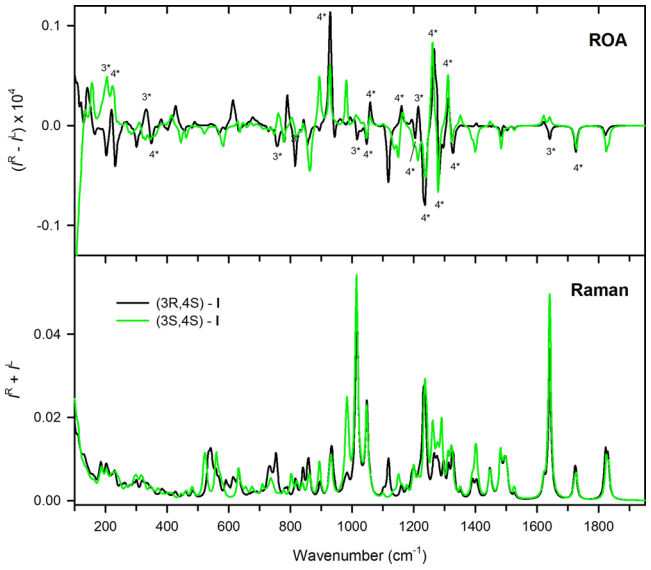

Figure 11. Calculated Raman and ROA spectra of the (3*R*,4*S*)-**I** (black) and (3*S*,4*S*)-**I** (green) diastereomers. Vibrational bands sensitive to the chirality on either C3 or C4 of the azetidine ring are labeled.

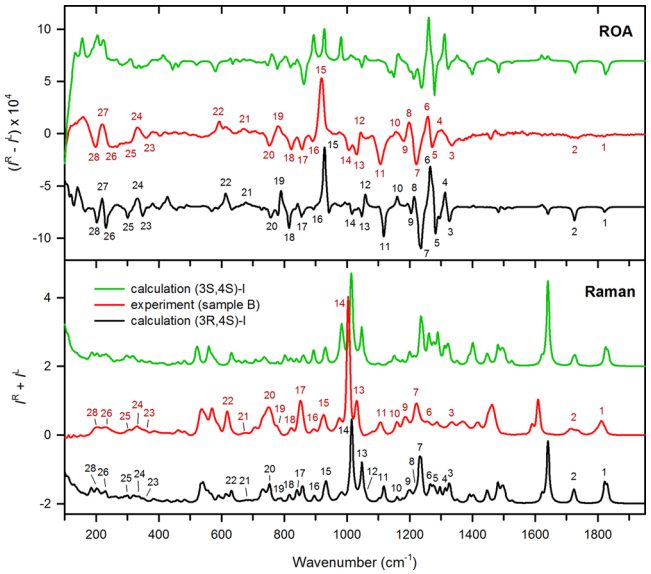

Figure 12. Comparison of the experimental (sample B) and simulated Raman and ROA spectra of (3*R*,4*S*)-**I** and (3*S*,4*S*)-**I**.

(wavenumbers) are usually slightly upshifted, mostly due to the harmonic approximation used in the calculations. However, the calculated relative band intensities also differ slightly from the experimental ones, which is caused by neglecting some of the interactions with the surrounding solvent environment (using the implicit solvent model) and the use of other approximations within the simulation; nevertheless, these effects change the strongest ROA bands only in a minor way.

On the basis of the comparison between the calculated ROA spectra of both diastereoisomers, we can identify several bands sensitive to the particular chirality on C3 and C4 of the azetidine ring (see Figure 11). There is obvious disproportion between the number and intensity of features specific to the chirality on each atom, strongly in favor of C4 (3*:4* = 6:12). Such an imbalance could be explained by the conformational flexibility of the groups attached to both chiral atoms:[42] (i) the rigid conformation of the linkage between the azetidine ring and phenyl group attached at C4 (see angle α in Figure 5) may cause the presence of narrow intensive bands connected with a specific C4 chirality and (ii) the conformational flexibility of the TES group attached to C3 (see angle δ in Figure 5) could lead to a decrease in and even the cancelation of some corresponding spectral features.

The experimental and theoretical spectra are compared in the Figure 12. It is clear that sample B (in red, middle) is best represented by the model of the (3*R*,4*S*) chirality. Indeed, 28 bands (labeled in Figure 12) that were similar in ROA sign and relative intensity could be found within 150−1850 cm^{-1}.

Vibrational Analysis. Detailed vibrational analysis was performed for the (3*R*,4*S*)-**I** isomer. In total, there are 114 vibrational modes within the inspected spectral region of 200−1850 cm^{-1}. We focus on those used for assignment of the absolute configuration (labeled from 1 to 28), complemented with 12 modes pronounced in the Raman spectrum. The results are shown in Table 2.

The most intense bands, both in the Raman and ROA spectra, originate for vibrations of the phenyl or amide (both amide I and III) group. There is also a strong ROA signal due to bending vibrations of δ(C−H) at chiral atoms of the azetidine ring (C3 and C4) and its deformations (δ(CCC) and γ(CCC)). Bending vibrations of the methyl and methylene groups in the BOC and TES residues are visible in the Raman spectrum but less so in the ROA spectrum. Most probably, vibrational coupling among different methyls and methylenes produces a number of ROA bands of similar frequencies but variable signs, which eventually results in signal cancelation. The ROA signal in the low-frequency region (<500 cm^{-1}) is formed by skeletal deformations of the whole molecule and rotations of the methyls of the BOC and TES groups. Therefore, it is very specific for each configuration of **I**.

From the above analysis (Figure 11 and Table 2), we see that the chirality at C4 can be determined relatively reliably. On the other hand, the absolute configuration at C3 is more challenging, as there are only a limited number of ROA bands connected to it (modes 8, 14, 20, 24, and 28) and they are weak. Nevertheless, the correspondence between the experimental and calculated spectra is good enough to conclude that sample B possesses the (3*R*,4*S*) chirality.

CONCLUSIONS

Our task was to investigate whether ROA spectroscopy can reliably discriminate between the different diastereoisomers of a taxol precursor. Indeed, combining the ROA experiment with theoretical simulations of the spectra, we have been able to assign absolute configurations of test samples A and B as (3*S*,4*R*)-**I** and (3*R*,4*S*)-**I**, respectively, with a high degree of confidence. Thus, ROA spectra can be used as a reliable tool for inspection of chirality during the synthesis of paclitaxel.

The diastereomers can be distinguished as well, although they are more challenging than mere enantiomers and their ROA spectra are not related by mere "mirror symmetry". On the other hand, diastereoisomeric Raman spectra do differ as well and can complement the ROA analysis, unlike those for the enantiomers. We also saw that such analyses are impossible without investigating molecular flexibility and complete averaging of all low-energy conformers. Although the ROA spectra were differently sensitive to the absolute configuration at the two chiral centers, the simulations were accurate enough to discriminate the diastereoisomeric species on the basis of comparison of the simulated and experimental spectra. Still,

DOI: 10.1021/acs.jpcb.6b12318
J. Phys. Chem. B 2017, 121, 1544−1551

Table 2. Calculated and Experimental Vibrational Frequencies in (3*R*, 4*S*)-I and Mode Assignment[a,b,c,d]

mode	DFT, ν (cm^{-1})	exp Raman, ν (cm^{-1})	exp ROA, ν (cm^{-1})	chiral sensitivity	assignment
1	1823	1811 m	1808 vw		ν(C═O), AZ
2	1726	1732, 1711 w	1734, 1711 vw	4*	ν(C═O), BOC-amide I
	1640	1610 m	ø	3*	ν(C═C), Ph, ν_{8a}
	1621	1590 w	ø		ν(C═C), Ph, ν_{8b}
	1500	1462 m	1473 w		δ(C−H_3) asymm., TES
	1481	1450 sh	1452 w		δ(C−H_3) asymm., BOC
	1450	1416 w	ø		δ(C−H_2) sciss., TES
	1395	1369 w	1371 vw		δ(C−H) bend., AZ + ν(C═C), Ph, ν_3
3	1326	1334 w	1337 w	4*	Amide III + δ(C−H) bend., AZ
4	1312	ø	1302 w	4*	ν(C═C), Ph, ν_{14} + δ(C−H) bend., AZ
	1296	1286 w	ø		Amide III + δ(C−H) bend., AZ
5	1282	ø	1272 m	4*	Amide III + δ(C−H) bend., AZ
6	1264	1256 vw	1258 m	4*	Amide III + δ(C−H) bend., AZ
7	1235	1221 m	1221 s	4*	δ(C−H), Ph + δ(C−H) bend. at C4, AZ
8	1213	ø	1197 m	3*	δ(C−H) bend. at C3, AZ + δ(C−H), Ph, ν_{9a}
9	1203	1185 w	1178 w	4*	ν(C−(CH_3) $_3$) symm., BOC + δ(C−H) bend. at C4, AZ + δ(C−H), Ph, ν_{9a}
10	1159	1159 w	1154 w	4*	ν(C−O−*t*Bu) asymm., BOC
11	1117	1105 w	1103 s		δ(C−H), Ph, ν_{18b} + δ(C−H) bend., δ(N−C), AZ
	1101	1080 vw	1080 w		δ(C−H), Ph, ν_{18b}
12	1058	ø	1043 w	4*	δ(C−H_3) wag., BOC
13	1048	1030 m	1030 m	4*	δ(C−H), Ph, ν_{18a}
14	1015	1004 s	1005 m	3*	δ(C−H), Ph, ν_{12}
	982	975 w	ø		δ(C−H_2) wag. & twist, δ(C−H_3), TES
15	929	925 m	919 s	4*	δ(C−H_3), BOC + δ(C−H), Ph, ν_{13}
16	894	894 vw	890 w		γ(CCC), AZ + γ(C−H), Ph, ν_{10b}
17	859	852 m	855 m		γ(C−H), Ph, ν_{10b} + δ(CCC), AZ
18	815	823 w	821 m		ν(C−(CH_3) $_3$), BOC + δ(CCC), AZ
19	788	777 sh	781 m		γ(C−H), Ph, ν_{10b} + γ(COO), BOC
20	755	751 m	752 m	3*	γ(C−H), Ph, ν_{11} + δ(CCC), AZ
	729	707 w	ø		γ(C−H), Ph, ν_{11} + δ(CCC), AZ
21	677	677 vw	670 w		δ(C−H_2) rock., δ(C−H_3), TES + δ(CCC), AZ
22	631	620 m	614 w		δ(CCC), Ph, ν_{6b}
	615	ø	592 m		γ(CCC), Ph, ν_{16b} + δ(CCC), AZ + ν(Si−(C_2H_5)$_3$), TES
	592	569 m	ø		γ(CCC), Ph, ν_{16b} + δ(CCC), AZ + ν(Si−(C_2H_5)$_3$), TES
	538	536 m	ø		γ(CCC), AZ
23	347	ø	357 w	4*	δ(C−(CH_3)$_3$), BOC
24	330	331 w	332 m	3*	γ(CCC), whole molecule
25	300	301 vw	304 m, sh		δ(Si−(C_2H_5)$_3$), TES
26	231	231 w	247 m		γ(CCC), whole molecule
27	219	ø	220 m	4*	γ(C−H_3), TES
28	201	202 w	196 m	3*	γ(C−H_3), TES

[a] s, strong (35−100%); m, medium (10−35%); w, weak (3−10%); vw, very weak (1−3%); ø, unrecognizable; sh, shoulder. [b] BOC, *t*-butyloxycarbonyl group; TES, triethylsilyloxy group; Ph, phenyl group; AZ, azetidinone. [c] ν, stretching; δ, in-plane deformation; γ, out-of-plane deformation. [d] ν_{xx}, numbering according to the Wilson benzene ring modes nomenclature.

computational errors stemming from conformer and solvent modeling should be carefully evaluated and need to be smaller for molecules with multiple chirality centers than for discriminations between two enantiomers only.

AUTHOR INFORMATION

Corresponding Authors

*E-mail: profant@karlov.mff.cuni.cz. Phone: +420 221911346 (V.P.).

*E-mail: bour@uochb.cas.cz. Phone: +420 220183348 (P.B.).

ORCID

Václav Profant: 0000-0001-8161-305X

Notes

The authors declare no competing financial interest.

ACKNOWLEDGMENTS

The work was supported by the Czech Grant Agency (16-05935S).

REFERENCES

(1) Saville, M. W.; Lietzau, J.; Pluda, J. M.; Wilson, W. H.; Humphrey, R. W.; Feigel, E.; Steinberg, S. M.; Broder, S.; Yarchoan, R.; Odom, J.; et al. Treatment of HIV-Associated Kaposi's Sarcoma with Paclitaxel. *Lancet* **1995**, *346*, 26−28.

(2) Wani, M. C.; Taylor, H. L.; Wall, M. E.; Coggon, P.; McPhail, A. T. Plant Antitumor Agents. VI. Isolation and Structure of Taxol, a Novel Antileukemic and Antitumor Agent from *Taxus Brevifolia*. *J. Am. Chem. Soc.* **1971**, *93*, 2325−2327.

(3) Schiff, P. B.; Fant, J.; Horwitz, S. B. Promotion of Microtubule Assembly in Vitro by Taxol. *Nature* **1979**, *277*, 665−667.

DOI: 10.1021/acs.jpcb.6b12318
J. Phys. Chem. B 2017, 121, 1544−1551

(4) Kingston, D. G. I. History and Chemistry. In *Paclitaxel in Cancer Treatment*; McGuire, W. P., Rowinski, E. K., Eds.; Marcel Dekker Inc.: New York, 1995; pp 1−34.
(5) Bharadwaj, R.; Yu, H. The Spindle Checkpoint, Aneuploidy, and Cancer. *Oncogene* **2004**, *23*, 2016−2027.
(6) Brito, D. A.; Yang, Z.; Rieder, C. L. Microtubules Do Not Promote Mitotic Slippage When the Spindle Assembly Checkpoint Cannot Be Satisfied. *J. Cell Biol.* **2008**, *182*, 623−629.
(7) Chiang, H. C.; Woods, M. C.; Nakadaira, Y.; Nakanishi, K. The Structures of Four New Taxinine Congeners, and a Photochemical Transannular Reaction. *Chem. Commun.* **1967**, 1201−1202.
(8) Holton, R. A.; Kim, H. B.; Somoza, C.; Liang, F.; Biediger, R. J.; Boatman, P. D.; Shindo, M.; Smith, C. C.; Kim, S. First Total Synthesis of Taxol. 2. Completion of the C and D Rings. *J. Am. Chem. Soc.* **1994**, *116*, 1599−1600.
(9) Nicolaou, K. C.; Yang, Z.; Liu, J. J.; Ueno, H.; Nantermet, P. G.; Guy, R. K.; Claiborne, C. F.; Renaud, J.; Couladouros, E. A.; Paulvannan, K.; et al. Total Synthesis of Taxol. *Nature* **1994**, *367*, 630−634.
(10) Masters, J. J.; Link, J. T.; Snyder, L. B.; Young, W. B.; Danishefsky, S. J. A Total Synthesis of Taxol. *Angew. Chem., Int. Ed. Engl.* **1995**, *34*, 1723−1726.
(11) Danishefsky, S. J.; Masters, J. J.; Young, W. B.; Link, J. T.; Snyder, L. B.; Magee, T. V.; Jung, D. K.; Isaacs, R. C. A.; Bornmann, W. G.; Alaimo, C. A.; et al. Total Synthesis of Baccatin III and Taxol. *J. Am. Chem. Soc.* **1996**, *118*, 2843−2859.
(12) Ojima, I.; Habus, I.; Zhao, M.; Zucco, M.; Park, Y. H.; Sun, C. M.; Brigaud, T. New and Efficient Approaches to the Semisynthesis of Taxol and Its C-13 Side Chain Analogs by Means of β-Lactam Synthon Method. *Tetrahedron* **1992**, *48*, 6985−7012.
(13) Barron, L. D.; Buckingham, A. D. Rayleigh and Raman Scattering from Optically Active Molecules. *Mol. Phys.* **1971**, *20*, 1111−1119.
(14) Barron, L. D.; Bogaard, M. P.; Buckingham, A. D. Differential Raman Scattering of Right and Left Circularly Polarized Light by Asymmetric Molecules. *Nature* **1973**, *241*, 113−114.
(15) Barron, L. D.; Bogaard, M. P.; Buckingham, A. D. Raman Scattering of Circularly Polarized Light by Optically Active Molecules. *J. Am. Chem. Soc.* **1973**, *95*, 603−605.
(16) Stephens, P. J. Theory of Vibrational Circular Dichroism. *J. Phys. Chem.* **1985**, *89*, 748−752.
(17) Buckingham, A. D.; Fowler, P. W.; Galwas, P. A. Velocity-Dependent Property Surfaces and the Theory of Vibrational Circular Dichroism. *Chem. Phys.* **1987**, *112*, 1−14.
(18) Nafie, L. A.; Freedman, T. B. Vibronic Coupling Theory of Infrared Vibrational Transitions. *J. Chem. Phys.* **1983**, *78*, 7108−7116.
(19) Barron, L. D.; Buckingham, A. D. Vibrational Optical Activity. *Chem. Phys. Lett.* **2010**, *492*, 199−213.
(20) Haesler, J.; Schindelholz, I.; Riguet, E.; Bochet, C. G.; Hug, W. Absolute Configuration of Chirally Deuterated Neopentane. *Nature* **2007**, *446*, 526−529.
(21) Parchaňský, V.; Kapitán, J.; Bouř, P. Inspecting Chiral Molecules by Raman Optical Activity Spectroscopy. *RSC Adv.* **2014**, *4*, 57125−57136.
(22) Parchaňský, V.; Kapitán, J.; Kaminský, J.; Šebestík, J.; Bouř, P. Ramachandran Plot for Alanine Dipeptide as Determined from Raman Optical Activity. *J. Phys. Chem. Lett.* **2013**, *4*, 2763−2768.
(23) Kapitán, J.; Baumruk, V.; Bouř, P. Demonstration of the Ring Conformation in Polyproline by the Raman Optical Activity. *J. Am. Chem. Soc.* **2006**, *128*, 2438−2443.
(24) Profant, V.; Baumruk, V.; Li, X.; Šafařík, M.; Bouř, P. Tracking of the Polyproline Folding by Density Functional Computations and Raman Optical Activity Spectra. *J. Phys. Chem. B* **2011**, *115*, 15079−15089.
(25) Profant, V.; Šafařík, M.; Bouř, P.; Baumruk, V. Raman Optical Activity Study of Poly-L-Proline Chains of Various Lengths. *Spectroscopy* **2010**, *24*, 213−217.
(26) Zhu, F.; Kapitán, J.; Tranter, G. E.; Pudney, P. D. A.; Isaacs, N. W.; Hecht, L.; Barron, L. D. Residual Structure in Disordered Peptides and Unfolded Proteins from Multivariate Analysis and Ab Initio Simulation of Raman Optical Activity Data. *Proteins: Struct., Funct., Bioinf.* **2008**, *70*, 823−833.
(27) McColl, I. H.; Blanch, E. W.; Gill, A. C.; Rhie, A. G. O.; Ritchie, M. A.; Hecht, L.; Nielsen, K.; Barron, L. D. A New Perspective on β-Sheet Structures Using Vibrational Raman Optical Activity: From Poly(L-Lysine) to the Prion Protein. *J. Am. Chem. Soc.* **2003**, *125*, 10019−10026.
(28) Blanch, E. W.; Kasarda, D. D.; Hecht, L.; Nielsen, K.; Barron, L. D. New Insight into the Solution Structures of Wheat Gluten Proteins from Raman Optical Activity. *Biochemistry* **2003**, *42*, 5665−5673.
(29) Bell, A. F.; Hecht, L.; Barron, L. D. Evidence for Global Mobility in the Premelting of a Polynucleotide from Temperature-Dependent Raman Optical Activity. *Biospectroscopy* **1998**, *4*, 107−111.
(30) Barron, L. D.; Zhu, F.; Hecht, L. Raman Optical Activity: An Incisive Probe of Chirality, and of Biomolecular Structure and Behaviour. *Vib. Spectrosc.* **2006**, *42*, 15−24.
(31) Barron, L. D.; Gargaro, A. R.; Wen, Z. Q. Vibrational Raman Optical Activity of Carbohydrates. *Carbohydr. Res.* **1991**, *210*, 39−49.
(32) Bell, A. F.; Hecht, L.; Barron, L. D. Low-Wavenumber Vibrational Raman Optical Activity of Carbohydrates. *J. Raman Spectrosc.* **1993**, *24*, 633−635.
(33) Yaffe, N. R.; Almond, A.; Blanch, E. W. A New Route to Carbohydrate Secondary and Tertiary Structure Using Raman Spectroscopy and Raman Optical Activity. *J. Am. Chem. Soc.* **2010**, *132*, 10654−10655.
(34) Blanch, E. W.; Hecht, L.; Syme, C. D.; Volpetti, V.; Lomonossoff, G. P.; Nielsen, K.; Barron, L. D. Molecular Structures of Viruses from Raman Optical Activity. *J. Gen. Virol.* **2002**, *83*, 2593−2600.
(35) Profant, V.; Pazderková, M.; Pazderka, T.; Maloň, P.; Baumruk, V. Relative Intensity Correction of Raman Optical Activity Spectra Facilitates Extending the Spectral Region. *J. Raman Spectrosc.* **2014**, *45*, 603−609.
(36) Frisch, M. J.; Trucks, G. W.; Schlegel, H. B.; Scuseria, G. E.; Robb, M. A.; Cheeseman, J. R.; Scalmani, G.; Barone, V.; Mennucci, B.; Petersson, G. A.; et al. *Gaussian 09*, revision B.01; Gaussian, Inc.: Wallingford, CT, 2009.
(37) Kim, K.; Jordan, K. D. Comparison of Density Functional and MP2 Calculations on the Water Monomer and Dimer. *J. Phys. Chem.* **1994**, *98*, 10089−10094.
(38) Stephens, P. J.; Devlin, F. J.; Chabalowski, C. F.; Frisch, M. J. Ab Initio Calculation of Vibrational Absorption and Circular Dichroism Spectra Using Density Functional Force Fields. *J. Phys. Chem.* **1994**, *98*, 11623−11627.
(39) Ditchfield, R.; Herhe, W. J.; Pople, J. A. Self-Consistent Molecular-Orbital Methods. IX. An Extended Gaussian-Type Basis for Molecular-Orbital Studies of Organic Molecules. *J. Chem. Phys.* **1971**, *54*, 724−728.
(40) Klamt, A.; Schüürmann, G. COSMO: A New Approach to Dielectric Screening in Solvents with Explicit Expressions for the Screening Energy and Its Gradient. *J. Chem. Soc., Perkin Trans. 2* **1993**, 799−805.
(41) Klamt, A. Cosmo and Cosmo-Rs. In *Encyclopedia of Computational Chemistry*; Schleyer, P. R., Allinger, N. L., Clark, T., Gasteiger, J., Kollman, P. A., Schaefer, H. F. I., Schreiner, P. R., Eds.; John Wiley & Sons: Chichester, U.K., 1998; pp 604−615.
(42) Kapitán, J.; Baumruk, V.; Kopecký, V.; Bouř, P. Conformational Flexibility of L-Alanine Zwitterion Determines Shapes of Raman and Raman Optical Activity Spectral Bands. *J. Phys. Chem. A* **2006**, *110*, 4689−4696.

DOI: 10.1021/acs.jpcb.6b12318
J. Phys. Chem. B 2017, 121, 1544−1551